SUPPLEMENTARY INFORMATION
https://doi.org/10.1038/s42256-019-0029-0

nature machine intelligence

In the format provided by the authors and unedited.

Autonomous functional movements in a tendon-driven limb via limited experience

Ali Marjaninejad[1,2], Darío Urbina-Meléndez[1], Brian A. Cohn[3] and Francisco J. Valero-Cuevas[1,2,3,4,5*]

[1]Department of Biomedical Engineering, University of Southern California, Los Angeles, CA, USA. [2]Ming Hsieh Department of Electrical and Computer Engineering, University of Southern California, Los Angeles, CA, USA. [3]Department of Computer Science, University of Southern California, Los Angeles, CA, USA. [4]Department of Aerospace & Mechanical Engineering, University of Southern California, Los Angeles, CA, USA. [5]Division of Biokinesiology & Physical Therapy, University of Southern California, Los Angeles, CA, USA. *e-mail: valero@usc.edu

nature machine intelligence

SUPPLEMENTARY INFORMATION
https://doi.org/10.1038/s42256-019-0029-0

In the format provided by the authors and unedited.

Autonomous functional movements in a tendon-driven limb via limited experience

Ali Marjaninejad [1,2], Darío Urbina-Meléndez [1], Brian A. Cohn [3] and Francisco J. Valero-Cuevas [1,2,3,4,5]*

[1]Department of Biomedical Engineering, University of Southern California, Los Angeles, CA, USA. [2]Ming Hsieh Department of Electrical and Computer Engineering, University of Southern California, Los Angeles, CA, USA. [3]Department of Computer Science, University of Southern California, Los Angeles, CA, USA. [4]Department of Aerospace & Mechanical Engineering, University of Southern California, Los Angeles, CA, USA. [5]Division of Biokinesiology & Physical Therapy, University of Southern California, Los Angeles, CA, USA. *e-mail: valero@usc.edu

nature machine intelligence

Supplementary Information for

Autonomous Functional Movements in a Tendon-driven Limb via Limited Experience

.

Ali Marjaninejad[1,2], Darío Urbina-Meléndez[1],
Brian A. Cohn[4], Francisco J. Valero-Cuevas[1,2,3,4,5,*]

correspondence to: valero@usc.edu

This PDF file includes:

Supplementary Materials and Methods
Supplementary Discussion
Supplementary Figures 1 to 7
Captions for Supplementary Videos 1 and 2

Supplementary Materials and Methods

Poincaré orbital stability analysis

We found that the system returned to its steady state cyclical movements within ~1 cycle after a manual perturbation (see Supplementary Figure 5 and 6, and Supplementary Video 2). However, we used Floquet multipliers to quantify the orbital stability of the steady state behavior after the perturbation [Methods-only reference 3]. The perturbation experiment consisted of 50 independent runs of 20 cycle each, where a manual perturbation was applied between the end of the 9th and beginning of 10th cycles. We extracted the 12th to the 20th cycles (as the system returned to its cyclical movement around the 11th cycle), interpolated those data, and resampled by a factor of 10 to increase our sampling rate without injecting noise. Thus, each of the 8 cycles now consisted of 800 (80*10) points sampled at ~780 s/s, corresponding to 1-100% of the cycle. For each percent of the gait cycle, Poincaré maps defined by the Poincaré section is defined as [Methods-only reference 3]:

$$\boldsymbol{S}_{k+1} = \boldsymbol{F}(\boldsymbol{S}_k) \qquad \text{Supplementary Equation 1}$$

where $\boldsymbol{S_k}$ is the state vector of the system ($\boldsymbol{q_1}$, and $\boldsymbol{q_2}$ in this study) for the kth cycle. Next, we define the linear approximation of Supplementary Equation 1 as:

$$(\boldsymbol{S}_{k+1} - S^*) \approx \boldsymbol{J}(S^*)(\boldsymbol{S}_k - S^*) \qquad \text{Supplementary Equation 2}$$

where $\boldsymbol{J}(\boldsymbol{S}^*)$ is the Jacobian matrix at that Poincaré section at a fixed point $\boldsymbol{S}^*$. We used Linear Regression Model (LRM) approximation to calculate $\boldsymbol{J}(\boldsymbol{S}^*)$. Fixed points, $\boldsymbol{S}^*$, for each map are defined as the global average over all state vectors [Methods-only reference 3]. Here, for each run, we calculated $\boldsymbol{S_k}$ and $\boldsymbol{S_{k+1}}$ pairs within a run and concatenated $\boldsymbol{S_k}$ and $\boldsymbol{S_{k+1}}$ pairs across runs to create 350 pairs (7 pairs across 8 cycles, times 50 independent runs). We averaged $\boldsymbol{S}^*$ over all state vectors across all runs.

The Eigenvalues of this Jacobian ($\boldsymbol{\lambda_1}$and $\boldsymbol{\lambda_2}$) define the Floquet multipliers, whose magnitudes quantify how a small perturbation will grow or diminish for a given Poincaré section between consecutive cycles. If the magnitude of the greatest eigenvalue is < 1, then small perturbations will be attenuated. Supplementary Figure 6c shows the amplitude of eigenvalues for each phase of a cycle, all of which are < 1.

Physical system

CAD and Additive Manufacturing techniques

After the design process and validation were finalized (as detailed in the Methods), Computer Aided Design (CAD) software (Autodesk Fusion 360 - Autodesk, Inc. San Rafael, CA) was used to create a 3D model of the leg, its supporting carriage, and treadmill components. Then Additive Manufacturing (3D Printing; Ultimaker 3 - Ultimaker USA Inc.) was used to construct these parts with PLA (polylactic acid)—white for the leg and black for components of the carriage and treadmill. PLA materials used only differ in color.

Treadmill

The treadmill belt was constructed with a strip of laminated nylon (.015’’ thick, Ozvinyl, McMaster-Carr, LA, CA, part 8810K41), which was sewn into a belt loop, and wound around two 3D-printed rollers).

Motors

DC brushless motors were mounted on the carriage with adequate ventilation (2342S024CR, Faulhaber, MICROMO, Clearwater, FL).

Tendons

We used Zero-stretch fly lines (Piscifun, Knoxville, TN) for the tendons, which were attached to the motor shafts with shaft collars (3mm ID with set screw, McMaster-Carr, LA, CA, Part 57485K63).

Further mechanical considerations

The linear-bearing and slide rail used were the McMaster-Carr part 6004K13 and 6004K93. Carriage side walls need to be parallel to slide smoothly; to compensate for manufacturing imperfections, walls were designed to tolerate a slope of ± 2°.

Data acquisition

One encoder (CUI AMT203-V, Digi-Key part 102-2050-ND) was used for each joint. To record treadmill band displacement, an incremental encoder was affixed to the forward roller pin (Arduino and CUI AMT103-V, Digi-Key part 102-1308-ND). To make data equi-sampled in time domain before calculating kinematics, we interpolated data (both joint angles and motor activation values) based on the time tags registered by the Arduino. For power measurement we used an Arduino and an INA219 sensor (Texas instruments. Dallas, TX)

Simulations

The Newton-Euler method was used (which involves balancing the angular momentum of the system), under the equation described below:

$$\vec{M}_{/0} = \vec{r}_{G1/0} \times -m_1 g\hat{j} + \vec{r}_{G2/0} \times -m_2 g\hat{j} + T_1\hat{k}$$

$$\dot{\vec{H}}_{/0} = \vec{r}_{G1/0} \times m_1\vec{a}_{G1} + I_1\vec{a}_1 + \vec{r}_{G2/0} \times m_2\vec{a}_{G2} + I_1\vec{a}_2$$

$$\vec{M}_{/1} = \vec{r}_{G2/1} \times -m_2 g\hat{j} + T_2\hat{k}$$

$$\dot{\vec{H}}_{/1} = \vec{r}_{G2/1} \times m_2\vec{a}_{G2} + I_2\vec{a}_2$$

where:

m_1, m_2	Masses of links 1 and 2
I_1, I_2	Inertia of links 1 and 2
g	Gravitational acceleration
$\vec{a}_1, \vec{a}_2$	Angular accelerations of links 1 and 2
$\vec{a}_{G1}, \vec{a}_{G2}$	Accelerations of links 1 and 2
T_1, T_2	External moment about point A
$\vec{M}_{/i}$	External moment about the ith joint
$\dot{\vec{H}}_{/i}$	Rate of change of angular momentum about the ith joint
$\vec{r}_{A/j}$	Position vector from point A to the ith joint
$\hat{\imath}, \hat{\jmath}, \hat{k}$	Unit vectors along x, y, and z axes
G_i	Center of mass for the ith link

The equations of motion result from setting the external moment equal to the rate of change of angular moment for each joint (Equations and code for the double pendulum simulation are adapted, with modifications, from [Methods-only reference 4]).

MATLAB's ode113 solver was used to simulate the differential equations of the system. The babbling data for the simulation was five minutes long with 500Hz sampling. More details on the parameters can be found online (see code availability statement). As referred to in the main paper, the results from the simulations are provided in Figures S2 and S3.

Supplementary Discussion

Biological inspiration for G2P

Individual vertebrates are under strong evolutionary pressure to learn and improve as much as possible from every experience during childhood (development) as well as throughout their entire lifespan to adapt to changes in their bodies, tasks, and environments. Vertebrates appear to use (i) trial-and-error[41], memory-based anticipation and kinematic/kinetic pattern recognition (e.g.,[50]), (ii) experience-based adaptation (e.g.,[51]), and when desired, (iii) cost-driven reinforcement learning[52]. Similarly, G2P first uses task-agnostic random inputs to create a general inverse map of its kinematics—similar to motor babbling and play in young vertebrates as in (i). Next, G2P considers all available data for potential refinements to a given inverse map even in the absence of explicit reward—as in (ii), and, if wanted, a higher-level controller can systematically maximize a reward by using some form of reinforcement learning—as in (iii). The refinement and reinforcement of a motor habit via continual exposure is also reminiscent of synaptic plasticity[53] that shapes specific patterns of neuronal connectivity by the Hebbian maxim *"neurons that fire together, wire together"*[54].

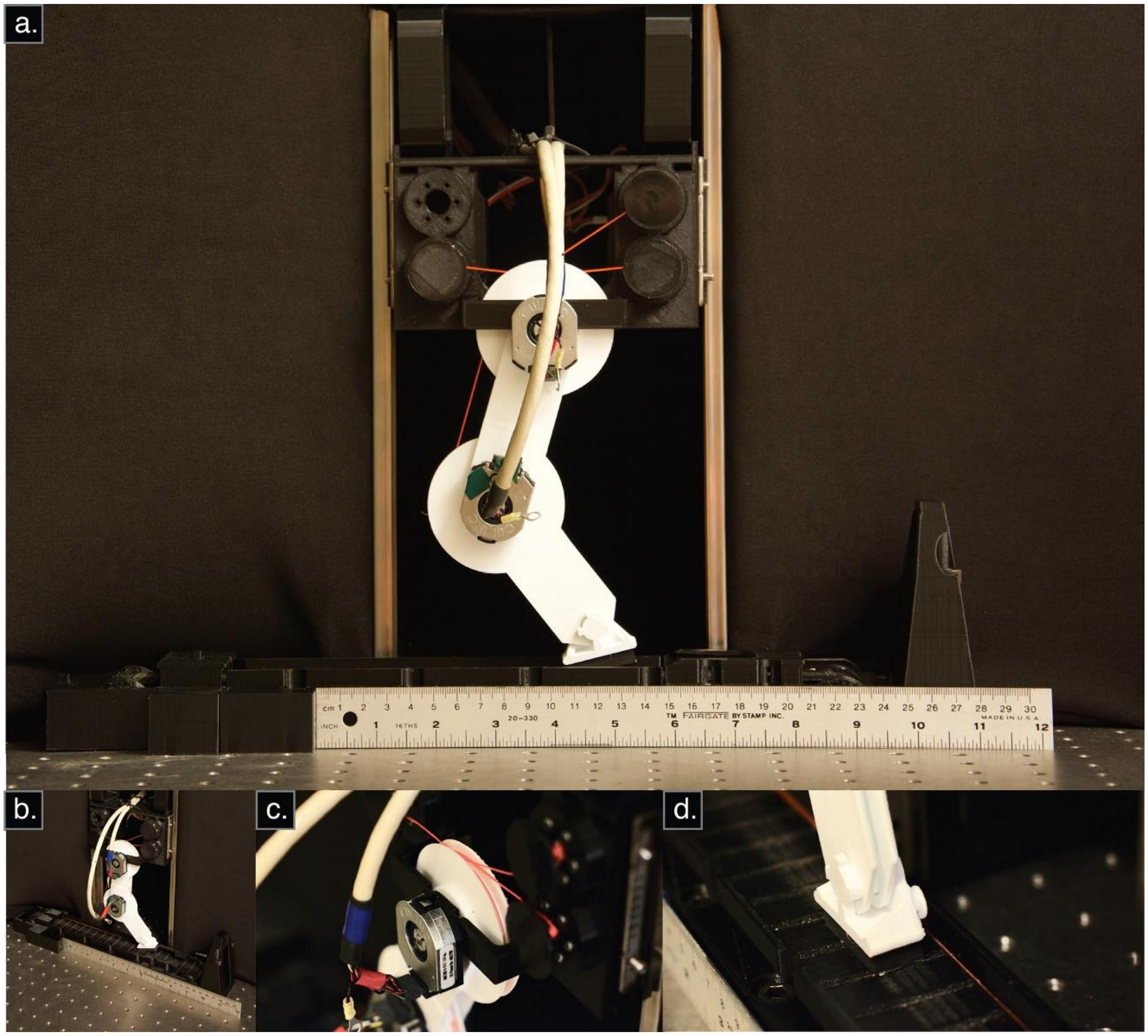

Supplementary Figure 1

The experimental apparatus (a) A sagittal view is shown with a ruler for scale. The limb is affixed to the carriage, which can be repositioned vertically. (b) When the carriage is lowered to allow contact with the treadmill, the limb can produce reward (by moving the belt towards the left). (c) The limb is actuated by three motors and the joint angles are monitored with encoders. (d) To improve contact area with the belt, the foot pad has a small rubber band connecting it to the distal link, yielding light dorsiflexion.

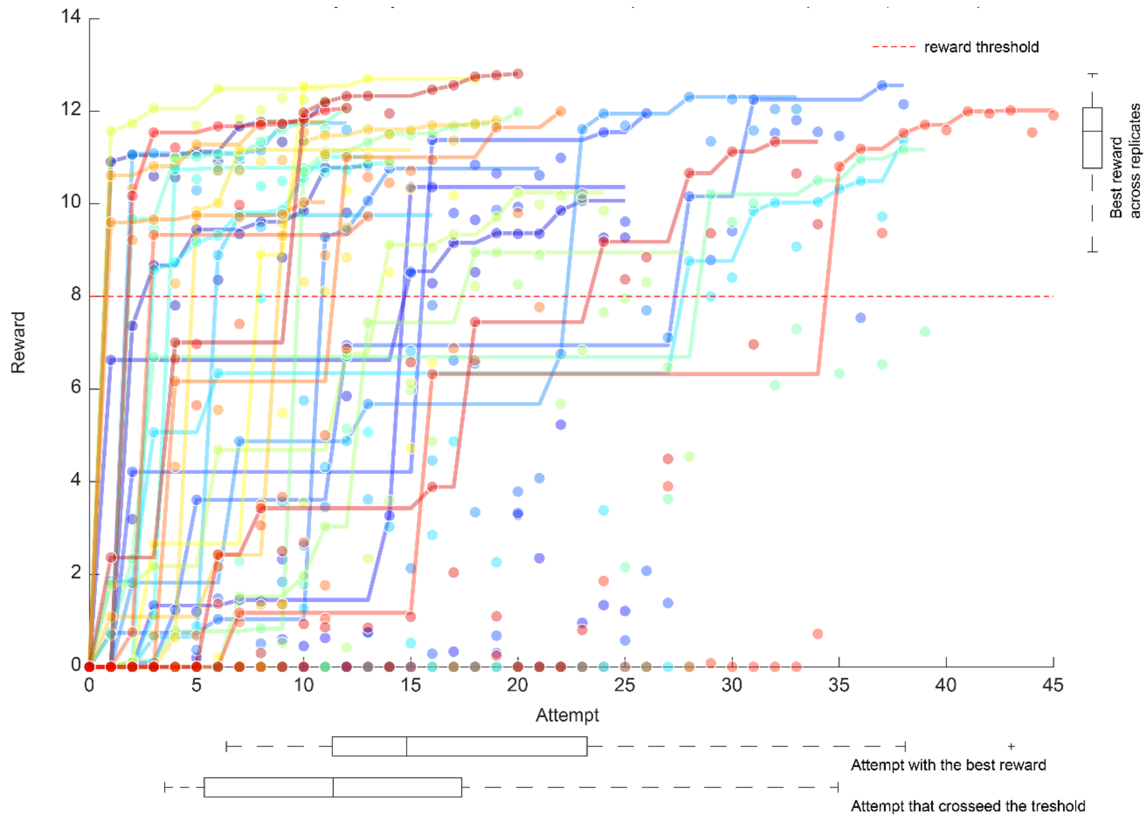

Supplementary Figure 2

Endpoint movement task results for simulation (preliminary work for experimental results in Figure 4a) Plot of reward as a function of attempt number for thirty independent runs. These simulations did not include a treadmill to propel. As an analogy to treadmill propulsion, the reward was defined as the amount of positive displacement of the limb's endpoint below the -1.75m line. The general pattern observed here is the same as the one on Figure 4a.

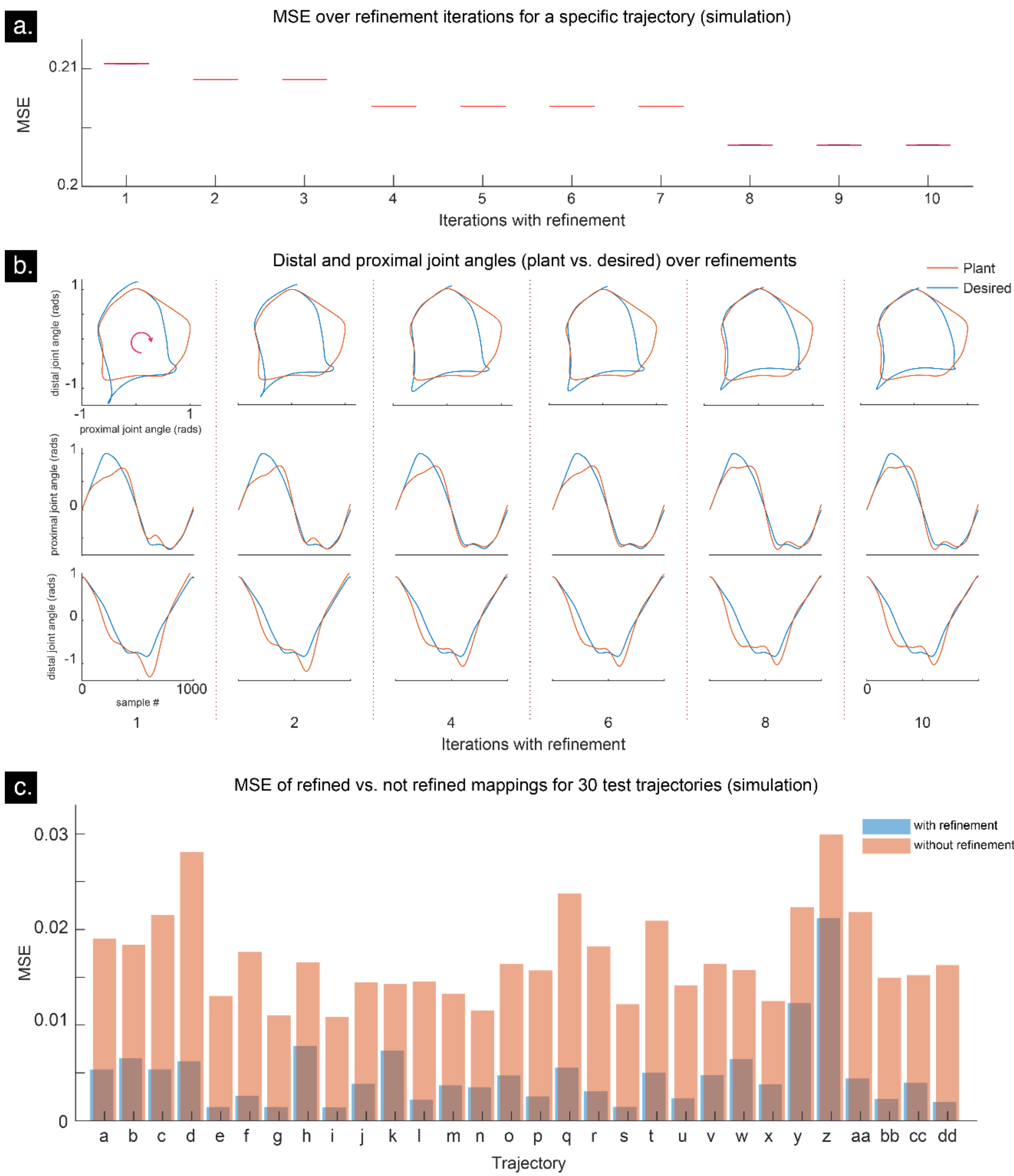

Supplementary Figure 3

Evaluation of trajectory tracking performance in simulation (preliminary work for experimental results in Figure 5a-b) (a) Mean Square Error (MSE) improvement for a specific trajectory as a function of number of refinements the system has performed on that trajectory. The inverse map is only updated if attempts improve the MSE also on the validation set (a random subset of the entire data—the same method as with the physical system). Unlike the data from the physical system (as in Figure 5a), the simulation has perfect replicability and hence the boxplots have no quartiles or whiskers. (b) Iterative refinements of the inverse map improve the inverse map the proximal and distal joint angles approach the trajectory defined by the target feature vector (similar to Figure 5a). (c). Test of simulated generalization of an inverse map across thirty unseen trajectories (similar to Figure 5b). Letters denote unique cyclical trajectories. No refinement is performed during the evaluation on these test-set trajectories.

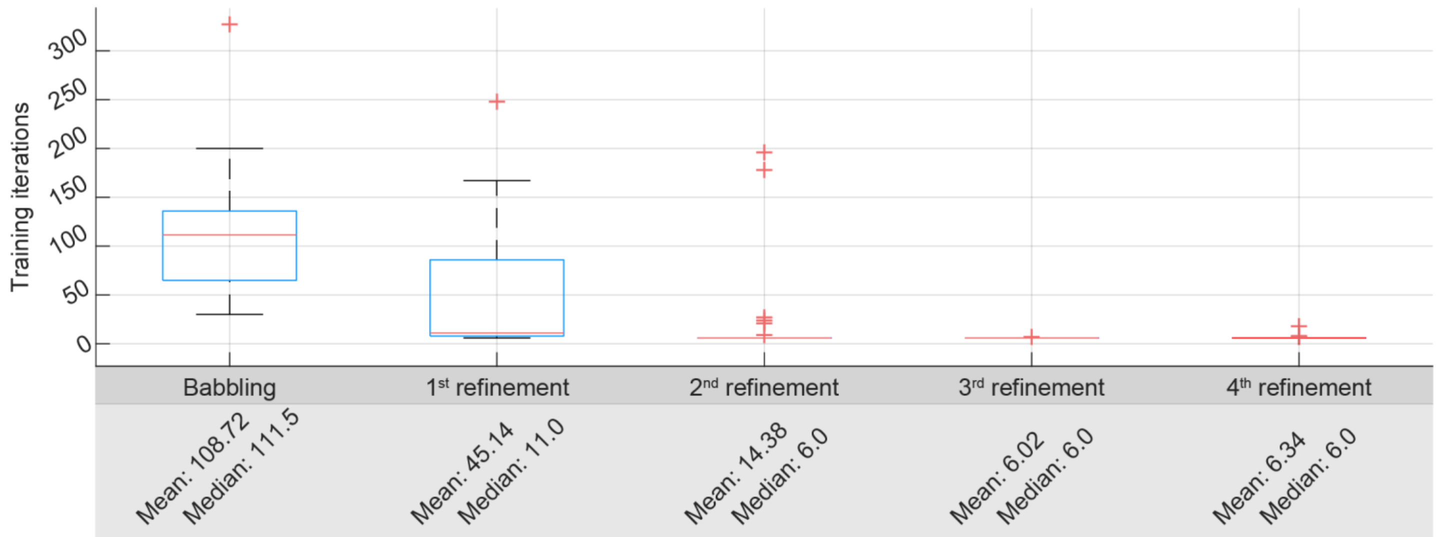

Supplementary Figure 4

Iterations needed for the ANN to converge This figure shows boxplots (for 50 independent runs) for training iterations over data from babbling and the first four refinements. Please note that the ANN converges in an average of 6 iterations after the 3rd refinement, which was the validation stopping criterion (see Methods). This shows that the inverse map has converged and does not get much more refined with more data from the exact same task.

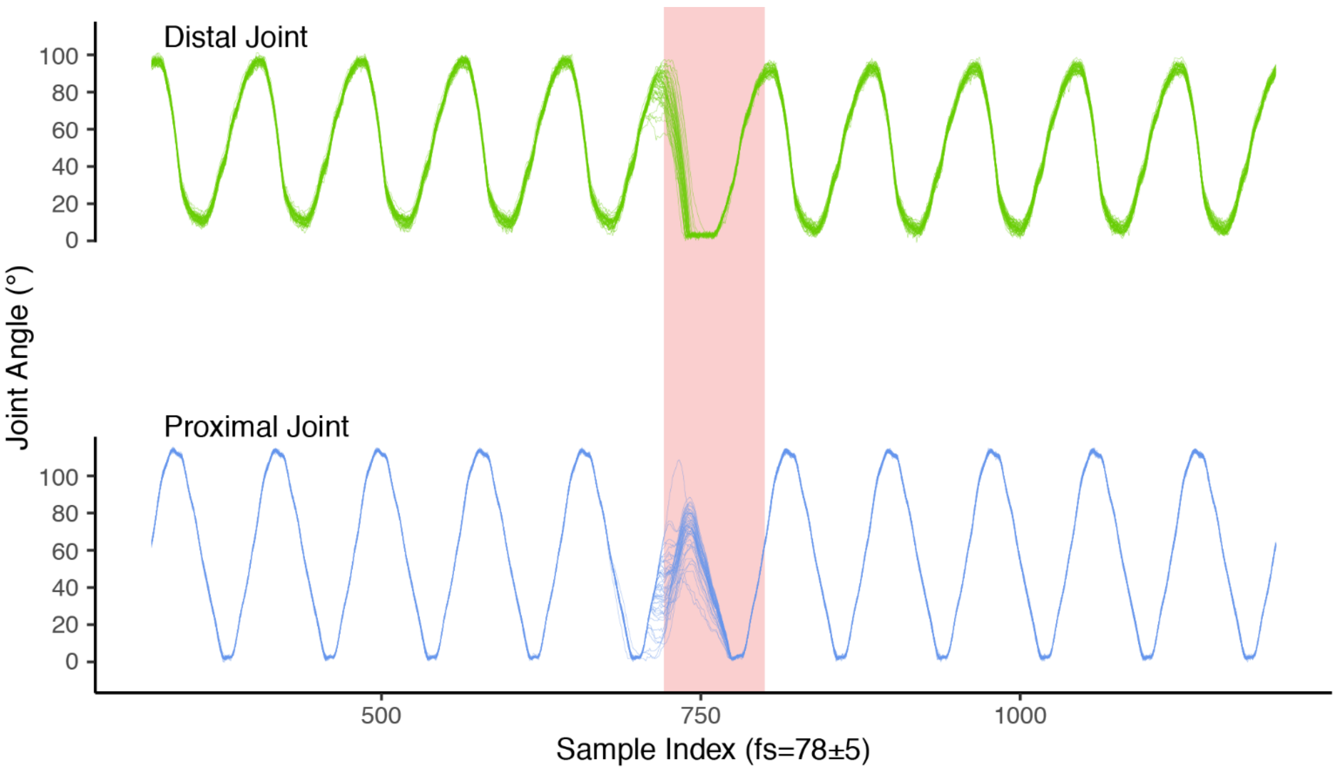

Supplementary Figure 5

Perturbation data for 50 independent tests Joint angles over the course of the 5th to the 15th cycles, where a manual perturbation was applied near the end of the 9th cycle (the 10th cycle is shaded). Joint angles are raw data, with no offsets subtracted to separate plots. Note the systems returns to the steady state cyclical movement within one cycle (see Supplementary Video 2).

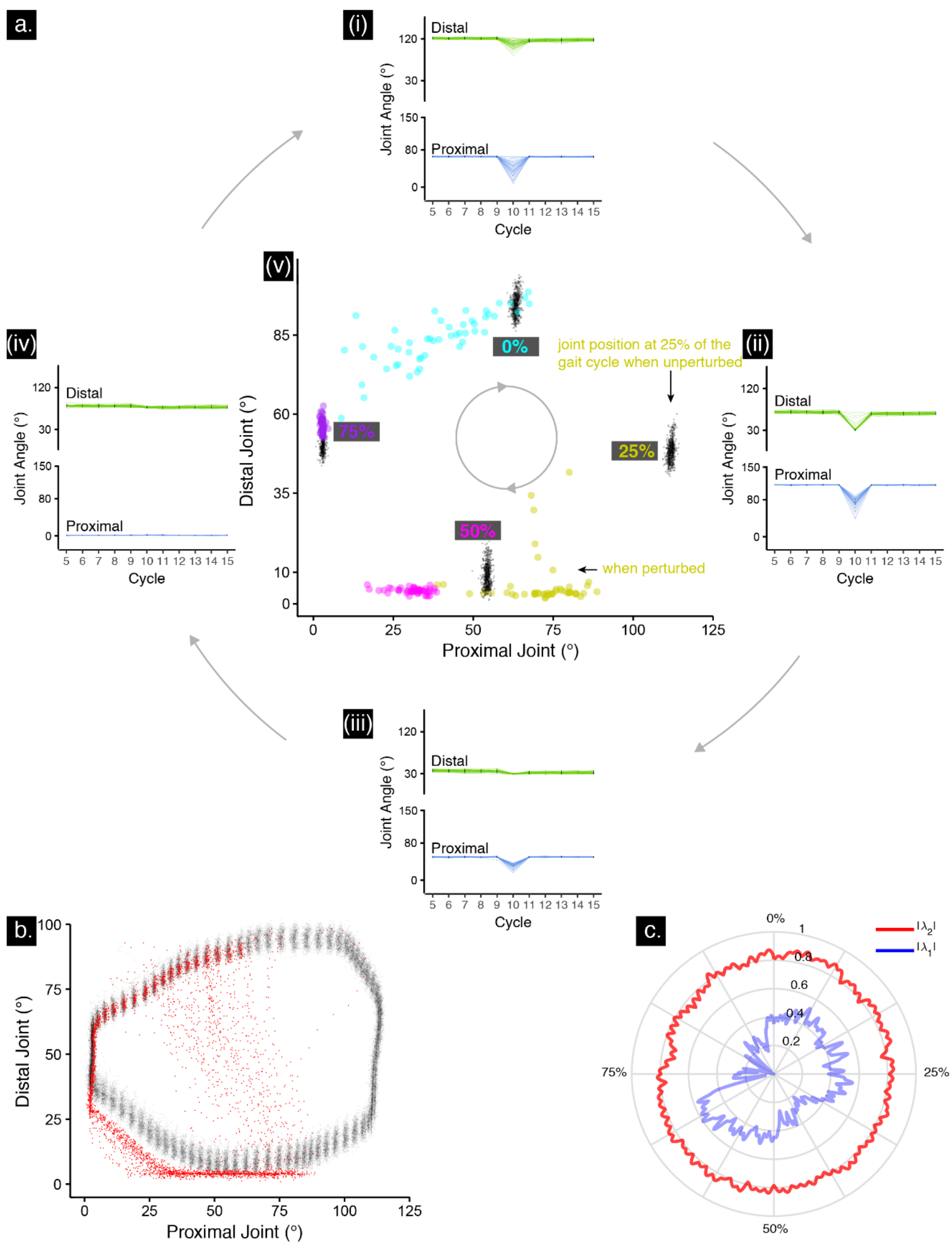

Supplementary Figure 6

Poincaré stability analysis (a-i-v) Poincaré return maps for 4 different points in the gait cycle (0%, 25%, 50%, and 75%). It takes ~1 cycle for these points to return to their stable location (crossing as a function of cycle in (i—iv), and angle-angle plots in (v), where the 10^{th} cycle is colored, and all other crossings are in black. (b) An angle-angle plot of the perturbation test (where the first 4 cycles were excluded to remove the effects of the initial position) with the 10^{th} cycle points in red. (c) Magnitude of the Floquet multipliers (eigenvalues of return map) for the orbital stability are all < 1.

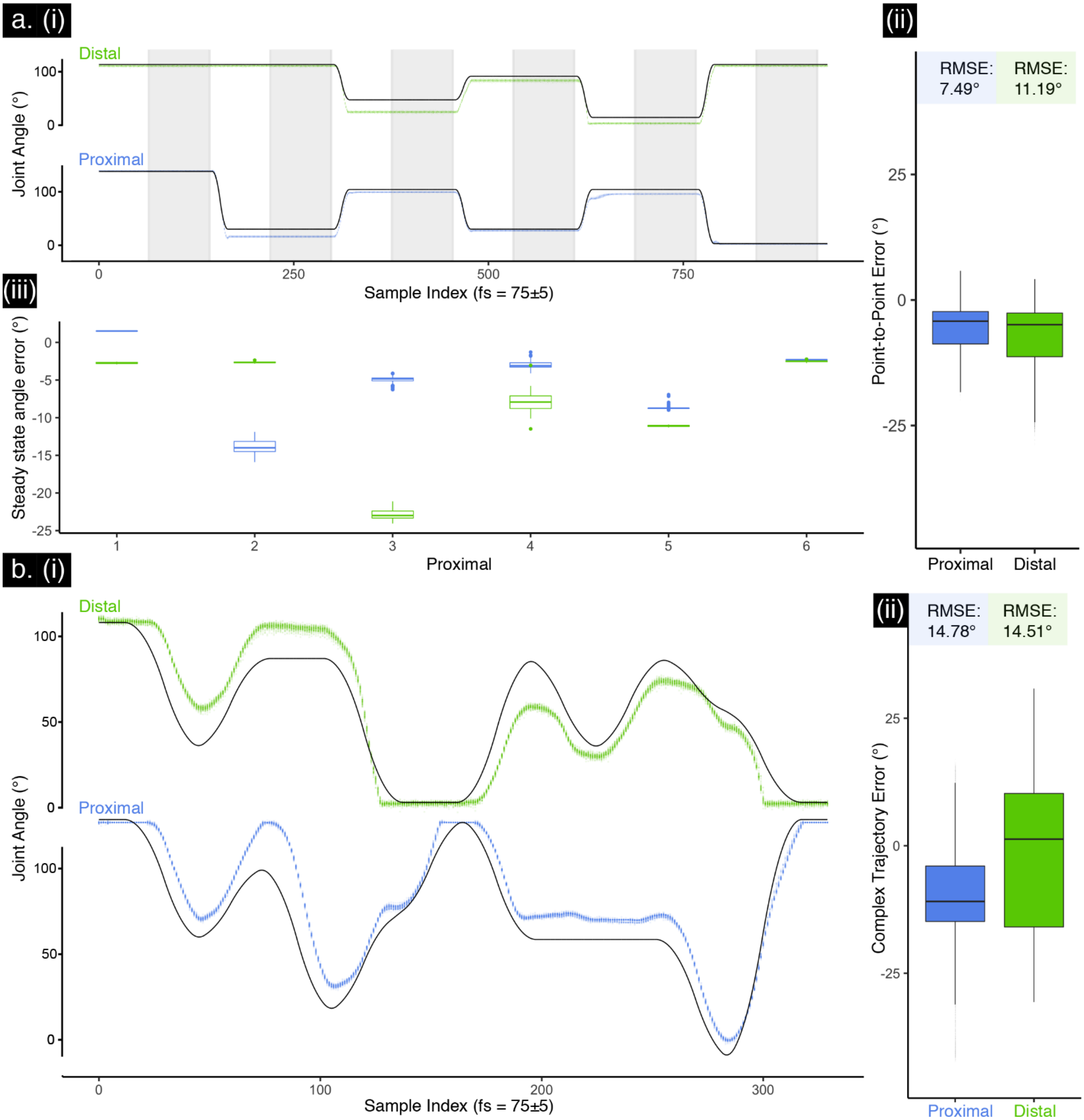

Supplementary Figure 7

System performance in point-to-point and more complex non-cyclical movements (a) Point-to-point movement: (a-i) Desired versus actual recordings from the proximal (blue) and distal (green) joints. (a-ii) Error boxplots and RSME values across all repetitions. (a-iii) Error boxplots for the second half of each hold phase (the grey sections in a-i; 78 samples) for each of the joints. Complex non-cyclical movement (b): (b-i) desired versus actual recordings from the proximal (blue) and distal (green) joints. (b-ii) Error boxplots and RSME values across all repetitions, for each of the joints.

Supplementary Video 1

Video of the system in Treadmill and Movements in air tasks First, the tendon-driven limb is introduced without tension to illustrate its lightweight double-pendulum design. Next, the video shows a streaming data visualization of motor babbling (an example is shown in Figure 6). This is followed by a demonstration of several attempts during an independent run (producing zero, low, and high treadmill rewards, as reported in Figure 4). Each independent run converges to a functional habit that produces the best reward for that run (without claim to uniqueness nor optimality). Finally, the G2P algorithm producing free cyclical movements in air (as shown in Figure 5a) is shown.

Supplementary Video 2

Videos of Supplemental Experiments: Perturbation, point-to-point and complex non-cyclical movements (a) Perturbation test: we manually struck the limb with a metal rod at the end of the 9^{th} steady state cycle. The system returns to steady behavior after ~1 cycle (see Supplementary Figures 5 and 6). (b) Point-to-point movements: the system first goes to an initial position. Then, it performs ramp-and-hold movements to 5 different postures. (c) More complex non-cyclical movements: the system follows a non-cyclical trajectory consisting of both ramp-and-hold, and smooth movements (both in-phase and out of phase across joints).